VALIDATION STUDY OF CFD ANALYSIS FOR HIGH-LIFT SYSTEMS

Mitsuhiro MURAYAMA, Yuzuru YOKOKAWA and Kazuomi YAMAMOTO
Aviation Program Group, Japan Aerospace Exploration Agency

Keywords: *High-Lift Configuration, CFD*

Abstract

In this study, three-dimensional flow computations around a simplified three-element high-lift configuration and a realistic high-lift configuration with a nacelle-pylon are performed. By comparison with the results, problems associated with the realistic configuration are clarified and the ways to improve the reliability of CFD methods are discussed in simulating the flows around high-lift devices. The simplified three-element trapezoidal wing model tested at NASA Langley and Ames is computed using both multi-block structured and unstructured mesh method and the mesh dependency is discussed. Importance of the mesh resolution to resolve the separated corner flows near the wing-fuselage junction is shown to improve the accuracy of computational results. Computations of the realistic configuration model tested at JAXA are performed using the unstructured mesh method and compared with the experimental data. Influences by the turbulent transition of the boundary layer and the presence of the nacelle-pylon on the aerodynamic forces are discussed.

1 Introduction

During the take-off and landing of an aircraft, performance of high-lift devices has strong impact on the operating costs and environments around airports, such as improvements of payload, fuel consumption, and noise emission [1-2]. Efficient high-lift devices with simplification of the structure are also expected to reduce the weight, production cost, and maintenance cost. CFD is expected to play an important role to develop the advanced high-lift devices. In the design process, precise prediction of the aerodynamic forces such as maximum lift, C_{Lmax}, and lift-to-drag ratio, L/D, is important. Prediction of the actual flight performance including Reynolds number effects is also an important issue. However, multi-element high-lift wing system that utilizes leading-edge slats and trailing-edge flaps complicates the flow features due to boundary layer transition, flow separation, interaction of wake of each element, and so on. Efforts to improve CFD for the high-lift systems are required in conjunction with experiments [3-6].

Basic CFD validation studies on two-dimensional or simplified three-dimensional high-lift configurations are important. In our previous works, validation studies have been conducted for two- and three-dimensional high-lift configurations using several CFD codes based on two different mesh systems, multi-block structured and unstructured mesh [7-10]. On the other hand, in the three-dimensional analysis on a realistic configuration with nacelle-pylon mounted under the wing, the interferences are also important phenomena to be resolved. By the presence of the engine, the high-lift devices are divided into several parts. The aerodynamic performance is often affected by the onset of local flow separation. Three-dimensional phenomena on such a realistic configuration have to be understood well.

In NASA Langley, a series of simplified three-element trapezoidal high-lift wings with body pod have been tested and the experimental data are provided for validation and development of CFD methods for three-dimensional high-lift flows [11-15]. In Civil Transport Team of Japan Aerospace Exploration Agency (JAXA/CTT), a research program to

develop design technologies for advanced high-lift systems has been conducted. In the program, a wind tunnel test using an aircraft configuration deploying the high-lift devices with fuselage, nacelle-pylon and Flap Track Fairing (FTF) was conducted in October 2005 - February 2006 to increase the knowledge of high-lift flows over a realistic aircraft configuration, to improve the measurement technologies, and to provide the detailed and systematic experimental data which can be disclosed for CFD validation [16-19].

In this paper, three-dimensional flow computations around the simplified three-element trapezoidal wing configuration tested at NASA Langley and Ames and a realistic configuration with a nacelle-pylon tested at JAXA are performed to assess and improve CFD methods in simulating the flow around high-lift devices. Computations of the trapezoidal wing model are performed using multi-block structured and unstructured mesh method for help to validate the CFD methods. The mesh dependency is discussed in the comparison. Computations of the complex configuration model are performed using the unstructured mesh method. Influences by the turbulent transition of the boundary layer and the presence of the nacelle-pylon on the aerodynamic forces are discussed. By comparison with the results, problems associated with the realistic configuration are clarified and the ways to improve the reliability are discussed.

2 Flow Solver

As the flow solver on multi-block structured meshes, UPACS (Unified Platform for Aerospace Computational Simulation) is used, which is a standard CFD code for multi-block structured mesh in JAXA [20-21]. The flow solver is based on a cell-centered finite volume method. In this study, the third-order scheme of Roe's flux difference splitting for convection terms is used. Time integration is carried out using MFGS (Matrix Free Gauss-Seidel) implicit method [22]. The multi-block structured meshes are generated with commercial software, Gridgen.

As the unstructured mesh generator and flow solver, TAS (Tohoku university Aerodynamic Simulation) codes [23-24] are used in this study. TAS_Mesh is a mesh generator with graphical user interface (GUI) tools [25-27]. It can generate triangular surface mesh with the advancing front method [25] and tetrahedral volume mesh using Delaunay tetrahedral meshing [26], as well as hybrid volume mesh composed of tetrahedrons, prisms, and pyramids for viscous flows with high Reynolds number [27]. The unstructured surface meshing using isotropic triangles is semi-automatic and the volume mesh generation is fully automated. In TAS_Flow, Navier-Stokes equations are solved on the unstructured mesh by a cell-vertex finite volume method. HLLEW (Harten-Lax-vanLeer-Einfeldt-Wada) method [28] is used for the numerical flux computations. Second-order spatial accuracy is realized by a linear reconstruction of the primitive variables. LU-SGS (Lower/Upper Symmetric Gauss-Seidel) implicit method [29] is used for time integration.

In this study, Spalart-Allmaras one-equation turbulence model (SA) [30] has been used to simulate turbulent flows. Both UPACS and TAS employed SA model without the trip term for transition and the *ft2* function which intends to suppress production of eddy viscosity due to numerical error. The production of eddy viscosity starts with the free stream value. A variation of the model which reduces the eddy viscosity in the regions of high vorticity [31], is also used. In this study, a simple combination using the minimum of the vorticity $\Omega = \sqrt{2\Omega_{ij}\Omega_{ij}}$ and strain rate $\hat{S} = \sqrt{2s_{ij}s_{ij}}$ is utilized in the modification [31] as follows;

$$S = \Omega + \min(0, \hat{S} - \Omega) \qquad (1)$$

The modified model computes turbulent vortical flow without adding much dissipation to the vortex core.

Computations were carried out on Fujitsu PRIMEPOWER HPC2500 multi-processor, which is the main machine of Numerical Simulator III in JAXA [32].

3 Computational Results

3.1 Three-element Trapezoidal Wing with Body Pod

3.1.1 Model Geometry and Computational Conditions

A trapezoidal high-lift wing model which has a full-span slat and a half-span single-slotted flap [11-12] was computed both on multi-block structured and unstructured meshes. A series of the trapezoidal wing models were tested at the NASA Langley Research Center 14- by 12-Foot Subsonic Wind Tunnel in 1998 and the NASA Ames Research Center 12-Foot Pressure Wind Tunnel (PWT) in 1999. The wind tunnel tests using the models were performed to produce experimental data for validation and development of CFD methods for three-dimensional high-lift flows [11-12]. In this study, the experimental data at NASA Ames PWT are compared with the computational results. The test section has a 12-foot diameter circular cross section with four 4-foot-wide flat surfaces centered about the horizontal and vertical centerlines. A splitter plate is installed in the test section for the semi-span testing. A configuration with slat and flap settings for landing was computed in this study. The slat and flap deflections are 30° and 25°, respectively. The mean aerodynamic chord of the model, c, is 39.6 inches and the model semi-span is 85.1 inches. Aspect ratio of the wing, AR, is 4.56. The slat gap and slat height are 0.015c. The flap gap and flap overlap are 0.015c and 0.005c, respectively.

Figure 1 shows the computational meshes. Two multi-block structured meshes and an unstructured mesh were generated. The baseline multi-block structured mesh has about 9.8 million mesh points. The number of blocks is 848 blocks. The minimum spacing in the normal direction to the wing surface is $0.02/\sqrt{Re}$. A fine multi-block structured mesh which has about 8 times mesh points of the baseline multi-block structured mesh was also generated by adding mesh points in i, j, and k direction, uniformly. The minimum spacing in the normal direction to the wing surface is $0.01/\sqrt{Re}$. The unstructured mesh has about 13 million mesh points. The minimum spacing in the normal direction to the wing surface is $0.01/\sqrt{Re}$. Only one or two cells are placed on the blunt trailing-edges for the unstructured mesh, while about 6 cells are placed for the baseline structured mesh. For all meshes, the outer boundary is a semi-sphere whose radius is about 60c.

In the current computations, freestream Mach number, M_∞, is 0.15 and the Reynolds number, Re, is 15×10^6. Fully turbulent flows are assumed in the computations.

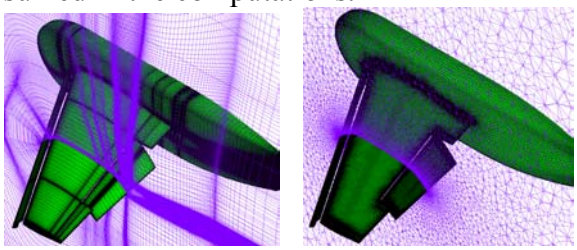

(a) Distant view (Left: Baseline structured mesh, Right: Unstructured mesh)

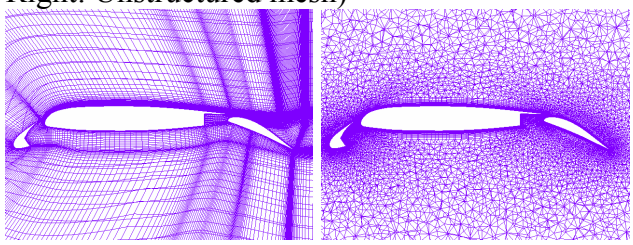

(b) Cross-sectional view at 50% span location (Left: Baseline structured mesh, Right: Unstructured mesh)

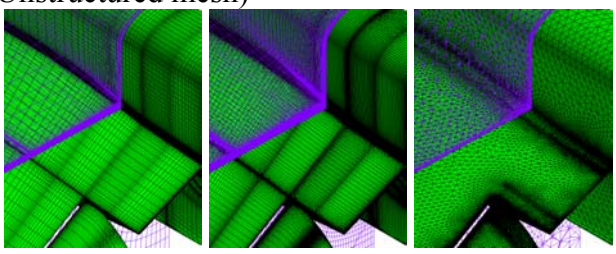

(c) Close-up view near the wing-body junction (Left: Baseline structured mesh, Center: Fine structured mesh, Right: Unstructured mesh)

Fig. 1 Computational meshes of part-span flap model

3.1.2 Computational Results

Figure 2 shows C_L-α and C_L-C_D for computed results on two structured meshes and an unstructured mesh, and uncorrected and

corrected experimental data [11-12]. C_L and C_D are lift and drag coefficients and α is angle of attack. As for C_L-α, all computational results show good agreement with the experimental data at the moderate angles of attack. All computational results predict slightly higher C_L than experimental results. A slight delay of stall angle of attack may be observed in our computations. The differences between computations by the baseline structured and unstructured meshes in C_L at the moderate angles of attack are about 1%, which is considered acceptable. However, at higher angles of attack (≥30°), the difference between computations by the baseline structured and unstructured meshes becomes larger. The result on the baseline structured mesh shows lower C_L. On the other hand, C_L predicted by finer structured mesh is slightly higher than those by the baseline structured mesh and closer to C_L by the unstructured mesh (≤ 1%).

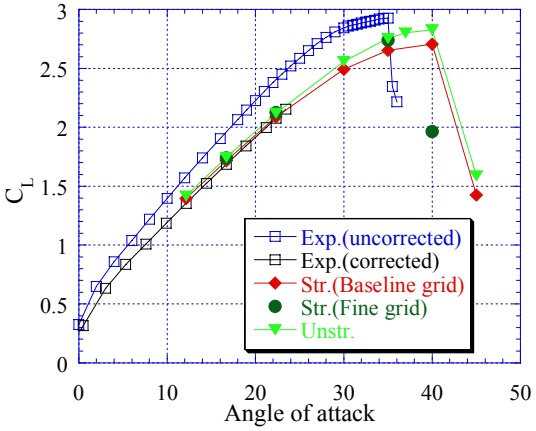

(a) C_L-α

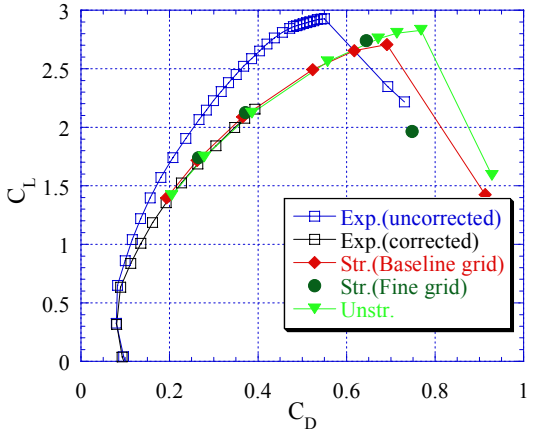

(b) C_L-C_D

Fig. 2 Comparison of C_L-α and C_L-C_D between experimental results and computational results

Figures 3-6 show the surface-restricted streamlines at angles of attack of 22.33°, 35°, 40°, and 45°. At angle of attack of 22.33°, all computational results in Fig. 3 show the similarity of the surface flow although a little difference can be found in the separated region near the wing-fuselage junction. At angle of attack of 35° where the result on the baseline structured mesh begins to show lower C_L than other results, the separated region on the baseline structured mesh near the wing-fuselage junction increases as shown in Fig. 4. At higher angle of attack of 40° where the computational results on the baseline structured and unstructured meshes show C_{Lmax} in Fig. 5, the separation increases on the baseline structured mesh. On the other hand, the results on the fine structured mesh show the similarity regarding the separation with the results of unstructured mesh. It seems that this excessive flow separation results from the insufficient mesh resolution. This excessive flow separation causes the reduction of C_L and it results in the difference with the fine structured and unstructured mesh results. On structured meshes, stretched elements in the spanwise direction are generally used. Therefore, the mesh resolution of the baseline structured mesh becomes relatively coarser at the juncture corner of the wing as shown in Fig. 1(c). The lack of the mesh resolution causes relatively larger separation on the computations. By refining the mesh, about 3% change in C_L is obtained. At angle of attack of 40°, the result on the fine structured mesh shows earlier stall than other results. The flow separates from the outer side of the slat and main wing on the fine structured mesh although the flow over the main wing remains attached on the other results. At angle of attack of 45° after the stall shown in Fig. 6, the computational results became unsteady and there was no steady state solution. However, it is found that both computational results on structured and unstructured meshes predict the same stall pattern.

As for C_L-C_D shown in Fig. 2(b), the overall level and the tendency of all computational results agree well with the wind-tunnel results. The differences in C_D between

computations by the baseline structured and unstructured meshes are about 100-200 drag counts, which is about 5 %. Improvement of the drag prediction for high-lift flows is one of the important issues to resolve.

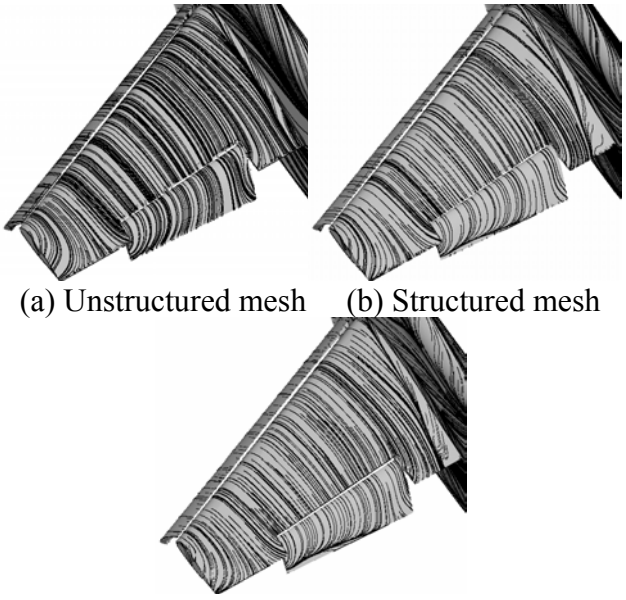

(a) Unstructured mesh (b) Structured mesh

(c) Fine structured mesh

Fig. 3 Surface restricted streamlines at α=22.33°

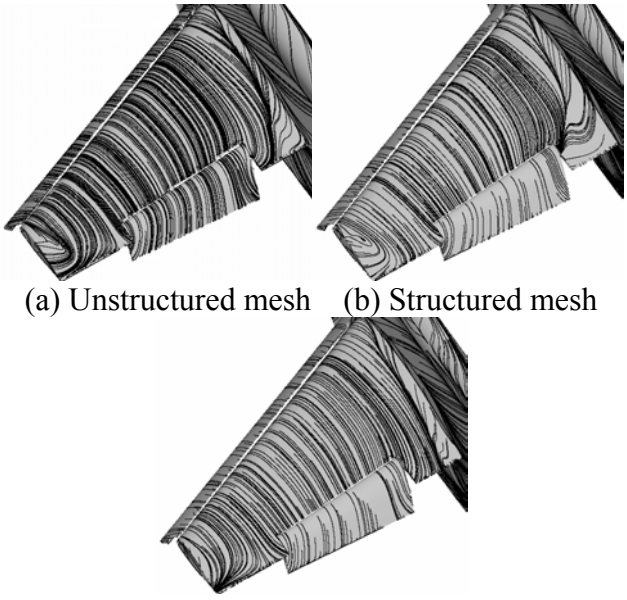

(a) Unstructured mesh (b) Structured mesh

(c) Fine structured mesh

Fig. 4 Surface restricted streamlines at α=35.00°

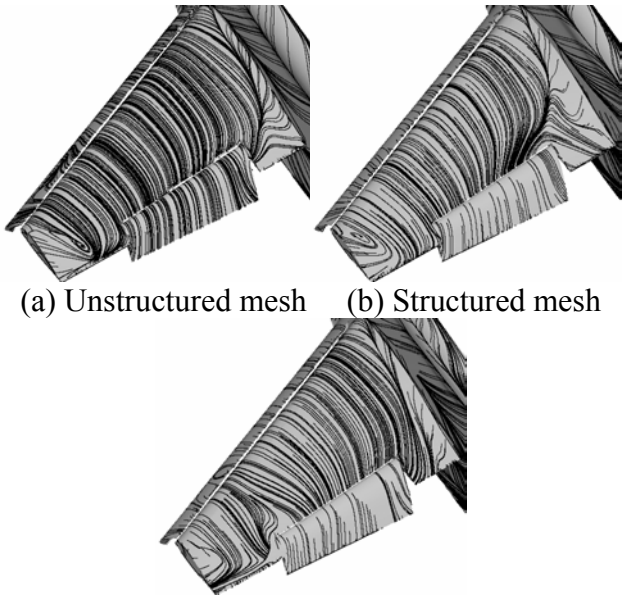

(a) Unstructured mesh (b) Structured mesh

(c) Fine structured mesh

Fig. 5 Surface restricted streamlines at α=40.00°

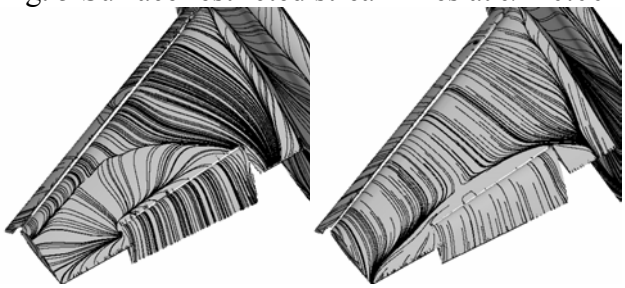

(a) Unstructured mesh (b) Structured mesh

Fig. 6 Surface restricted streamlines at α=45.00°

3.2 Landing Configuration Deploying High-Lift Devices with Nacelle-Pylon

3.2.1 Model Geometry and Computational Conditions

Figure 7 shows a wind tunnel model tested in October 2005 - February 2006 at JAXA 6.5m × 5.5m Low Speed Wind Tunnel (JAXA-LWT1) [16-18]. JAXA-LWT1 is a closed-circuit wind tunnel with an octagonal cross section. The test was carried out to provide the experimental data for CFD validation to know flow physics for realistic aircraft take-off and landing configurations deploying the high-lift devices. The model was designed assuming a 100-passenger class civil jet aircraft. The scale of the wind tunnel model is about 1/6 of the assumed aircraft. The lengths of the wing span and fuselage are 2.3m and 4.9m, respectively. The aspect ratio of the wing is 9.42 and the leading-

edge sweep angle is 33 degrees. The mean chord length of this model is 0.426*m* under the stowed configuration. The model has a leading-edge slat supported by eight slat supports, a double-slotted flap at inboard and a single-slotted flap at outboard with a circular fuselage, a flow-through nacelle-pylon mounted under the wing, and three Flap Track Fairings (FTF), as shown in Fig. 7. For the landing setting, the deflection angles of the slat, flap, and aft-flap are 25, 35, and 20 degrees, respectively.

In the testing, various kinds of measurements were conducted to verify CFD analysis in detail [16-18]. Five-component aerodynamic forces, surface pressure with pressure taps and Pressure Sensitive Paint (PSP), unsteady pressure, and velocity distribution around the model using Particle Image Velocimetry (PIV) were obtained. Surface flow visualization was carried out with tuft, oil flow and china clay to reveal the flow phenomena such as separation and transition. Aeroacoustic noise sources were also measured using phased array microphones [18].

Figure 8 shows the computational unstructured mesh. FTF and brackets to support the high-lift devices are removed in the computations. The unstructured mesh has about 6 million mesh points. The minimum spacing in the normal direction to the wing surface is $0.02/\sqrt{\mathrm{Re}}$. Only one or two cells are placed on the blunt trailing-edges.

In the current computations, freestream Mach number, M_∞, is 0.175 and the Reynolds number, *Re*, is 2.1×10^6 based on MAC. Two kinds of boundary layer conditions, fully turbulent flow and transient flow with laminar regions, were compared in the computation. The specified laminar regions were based on the experimental observations by the china-clay visualization. The laminar regions are shown in Fig. 9. In the experiments, the boundary layer on the lower surface of the main wing became turbulent locally by the influence of the slat supports and FTF. In the computations, the whole boundary layer on the lower surface of the main wing was assumed to be laminar.

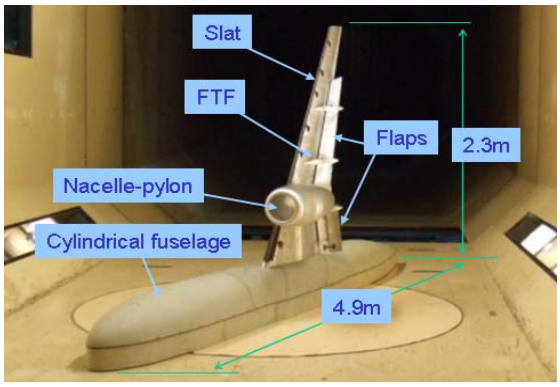

Fig. 7 Wind tunnel testing model in JAXA-LWT1 test section

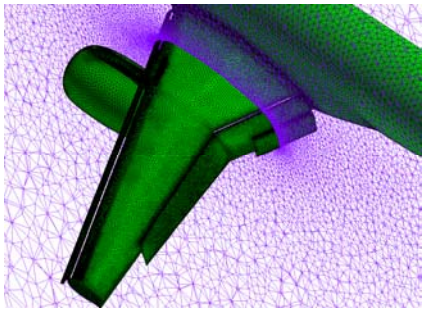

(a) Distant view

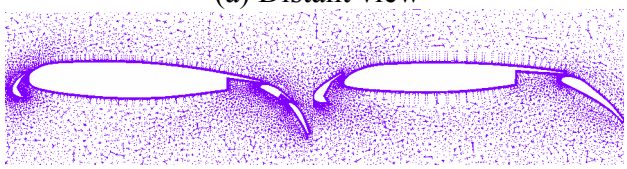

(b) Cross-sectional view (Left: an inboard span location, Right: an outboard span location)

Fig. 8 Computational mesh of JAXA wind tunnel model

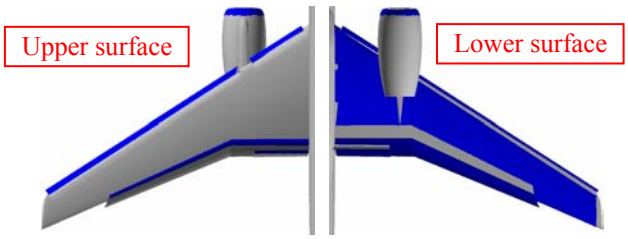

(a) α=5°

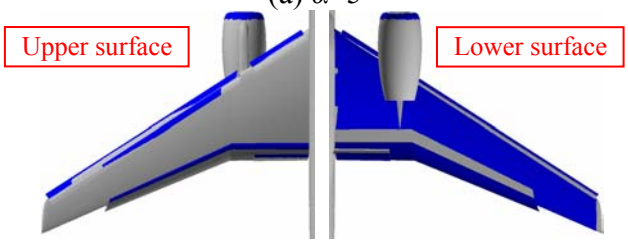

(b) α=10°

Fig. 9 Regions of turbulent transition of boundary layer assumed in computations (Blue: Laminar, Gray: Turbulent)

3.2.2 Computational Results

Figure 10 shows C_L-α, C_L-C_D, and C_M-α for computed results and experimental data after the correction of the wind tunnel wall and other interference where C_M is a pitching moment coefficient. In Fig. 10, the results of fully turbulent and transient flows with laminar regions are also compared. As for C_L-α, both computational results show good agreement with the experimental data at the moderate angles of attack before stall. Although the gradient of lift before stall has slight differences, computations could capture the whole characteristics. The stall angle of attack is also well captured in the computations although the rapid decrease of C_L after the stall shows different nature between the experimental and computational results. The results with laminar regions show higher C_L and better agreement with experimental results, especially at higher angles of attack.

As for C_M, the overall tendency of the computational results agrees well with the wind-tunnel results including the change of the gradient after the stall although the lower shift of C_M is seen in the computations. As for C_L-C_D, both computational results overestimate C_D. The differences are larger even before the stall compared with the trapezoidal wing case. It seems that this is mainly due to insufficient grid resolution against the complicated model geometry in the computations.

Figure 11 shows the locations of the cross sections for the static pressure measurement. Figures 12 and 13 show the comparisons of C_P at α = 5° and 10°. Large jumps of C_p near the trailing-edges of each element in the computations are derived from the lack of mesh resolution on the blunt trailing-edges. Both computational results show good agreement with experimental results at Section1 and Section5 in Figs, 12 and 13, except for the flap leading-edges. Designed wide and flat suction peaks near the leading-edge of the main-wing are well predicted. At α = 10°, the difference between the fully turbulent and specified transition flows is larger. The results of the specified transition flow show larger suction peaks by the acceleration of flow near the main and flap leading-edges and better agreement with results. Near the wing tip at Section7, the difference between experimental and computational results is slightly large, especially on the upper surface near the trailing-edge of the main-wing. This seems to be due to the difference in the separation patterns.

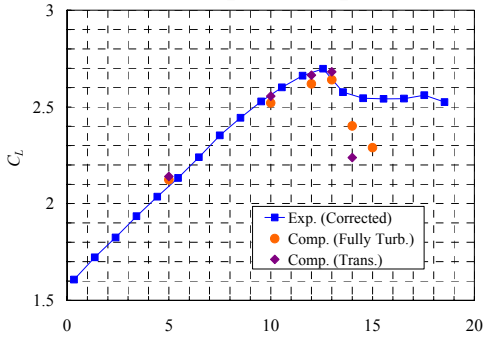

(a) C_L-α

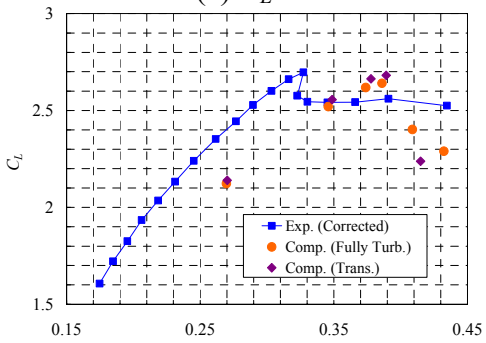

(b) C_L-C_D

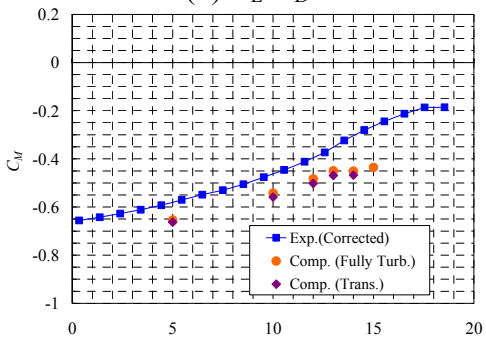

(c) C_M-α

Fig. 10 Comparison of C_L-α, C_L-C_D, and C_M-α between experimental and computational results

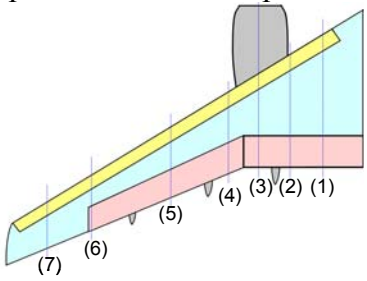

Fig. 11 Cross sections for static pressure measurement

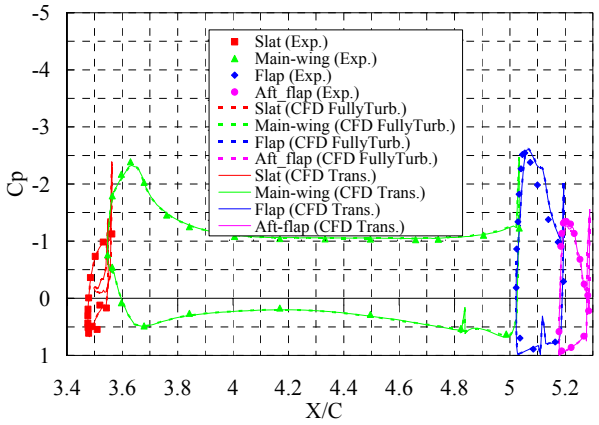

(a) Section 1

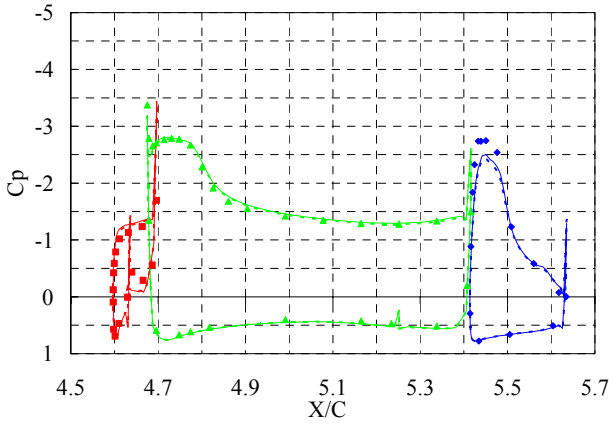

(b) Section 5

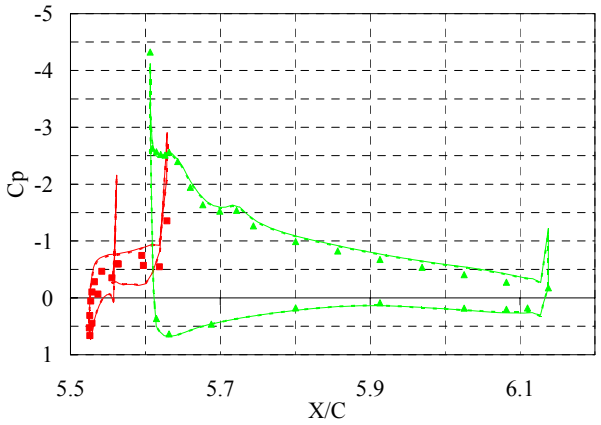

(c) Section 7

Fig. 12 Surface pressure distributions at α=5° (Experimental data is at α=4.43°)

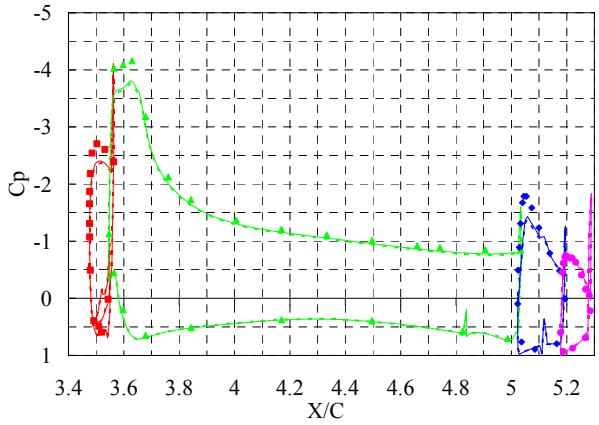

(a) Section 1

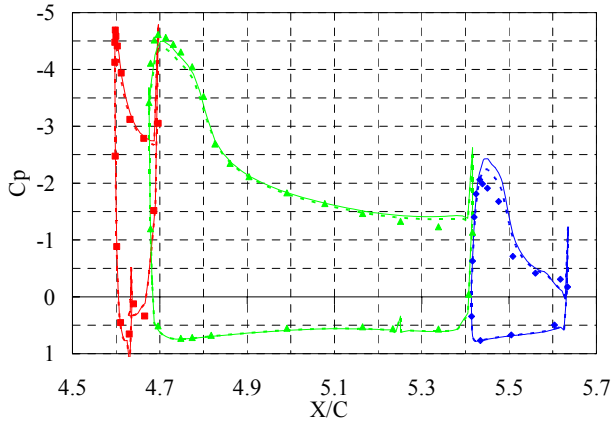

(b) Section 5

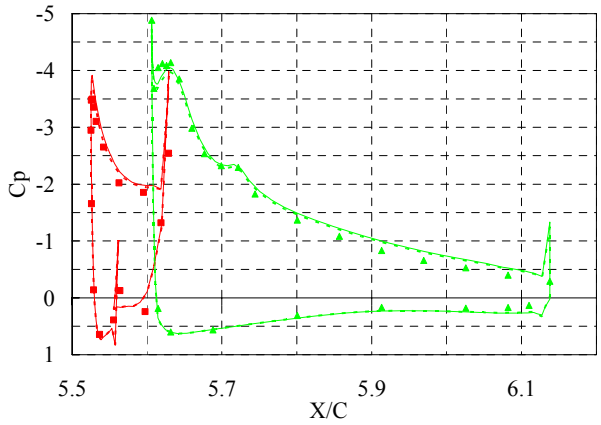

(c) Section 7

Fig. 13 Surface pressure distributions at α=12° (Experimental data is at α=12.57°)

Figures 14-16 compares the surface flow patterns between the experimental and computational results with specified laminar regions at α = 5°, 10°, and 15°. At a moderate angle of attack, α = 5°, the computational results show good agreement with the experimental results especially on the slats and the main-wing. The interference of the nacelle-pylon is small at this lower angle of attack. On the other hand, there are several local differences. The experimental result clearly shows the influence of the slat supports and FTF on the upper side of the main wing and flaps. Near the trailing-edge of the wing tip, only experimental result shows a little flow separation. It seems that the separation causes the disagreement of surface pressure distribution in Figs. 12(c) and 13(c). The difference of the surface flow on the flaps is relatively larger. The larger local flow separations by the influence of FTF appear on the flap. In addition, the experimental result shows the existence of laminar separation bubble near the leading-edge region, while the computational results do not show the laminar separation bubble although the laminar regions are assumed near the leading-edge in the computations. The present relatively coarse mesh resolution may be lack to capture the laminar separations.

At angle of attack of 10°, the difference between experimental and computational results becomes larger on the nacelle and near the wing tip. On the outboard side of the nacelle, the separation line in the experimental result locates former than in the computational result. In the present computations, the separated flow was not resolved well quantitatively. On the other hand, the difference of the flow separation near the wing tip seems to be produced by the presence of the slat supports.

Figure 16 shows the results at angle of attack of 15°. Large separation is visible on the main-wing after the nacelle-pylon in the experimental results. The separation affects the whole stall performance. Computational result also predicts the similar separation phenomena.

Figures 17-19 show the oil-flow and streamlines near the nacelle-pylon computed at α=10°, 13° and 14°. As the increase of angle of attack, the flow separation on the outboard side of the nacelle becomes larger and the separation line moves upstream. At the post-stall angle of attack of α=14°, the separation location moves further upstream. The separation at this location seems to have large impact on the stall. It seems that the inner side of the outboard slat does not work by the increased separation. The separated and reversed flow near the inner side of the outboard slat is one of the causes of the separation on the upper surface of the main wing after the nacelle, which affects the stall performance. The flow interacts with the leading-edge slat and the span-wise clearance gap of the discontinuous slat at the location where the nacelle-pylon is attached. The vortex and separation reduce C_L at the angle of attack. More precise prediction of these kinds of local separation is required for the computations of realistic high-lift configurations.

(a) Experimental result

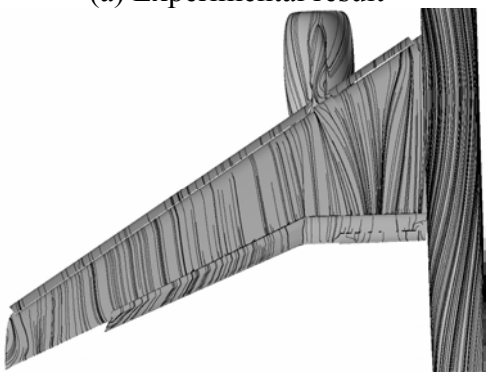

(b) Computational result

Fig. 14 Comparison of surface flow pattern at α=5° (Experimental data is at α=4.43°)

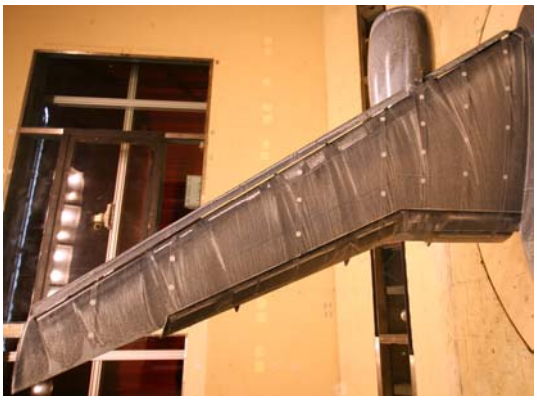

(a) Experimental result

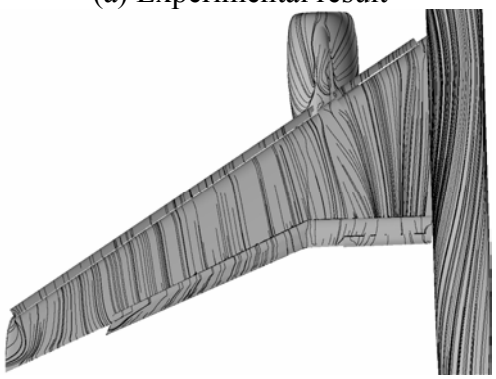

(b) Computational result

Fig. 15 Comparison of surface flow pattern at α=10° (Experimental data is at α=10.55°)

(a) Experimental result

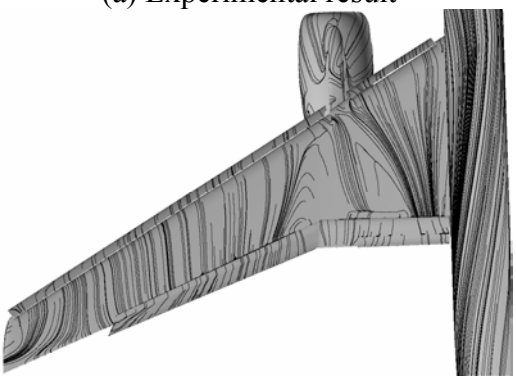

(b) Computational result

Fig. 16 Comparison of surface flow pattern at α=15° (Experimental data is at α=15.54°)

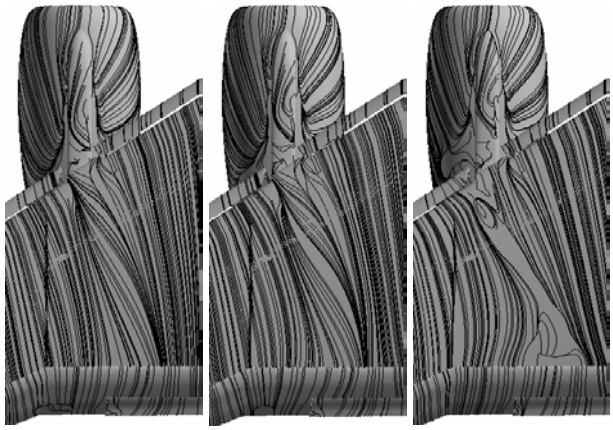

(a) α=10° (b) α=13° (c) α=14°

Fig. 17 Close-view of computed surface flow pattern near the nacelle

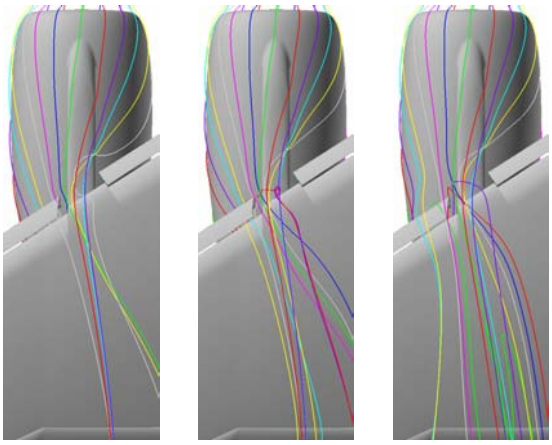

(a) α=10° (b) α=13° (c) α=14°

Fig. 18 Close-view of computed streamlines near the nacelle

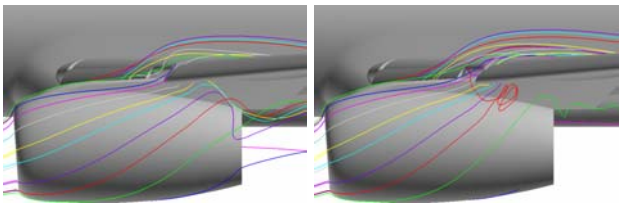

(a) α=10° (b) α=13°

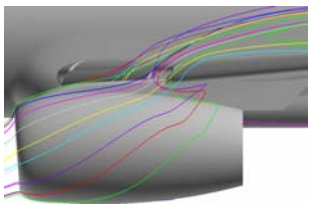

(c) α=14°

Fig. 19 Side-view of computed streamlines near the nacelle

4 Concluding Remarks

To improve the aerodynamic force prediction around high lift devices, flow computations around simplified and complicated three-element high-lift configurations were performed.

A simplified three-element trapezoidal wing model was computed using both multi-block structured and unstructured mesh method and the mesh dependency was discussed. Acceptable prediction of aerodynamic forces was obtained on both computations even for the stall prediction. The present computations showed good results for the basic high-lift configuration. In the configuration, importance of the mesh resolution to resolve the separated corner flows near the wing-fuselage junction was also shown to suppress the excessive separated flow and improve the computational results.

For a realistic high-lift configuration with a nacelle-pylon tested at JAXA, computational results agreed reasonably before the stall as for the lift prediction. The computational results with specified turbulent transition of boundary layer showed better agreement with the experimental results and the importance of the prediction of the transition. It was also shown that the vortex and separation generated by the interaction of flows due to the presence of the nacelle-pylon reduced C_L and affected the stall performance largely. In addition, the flow separations due to the slat supports and FTF on the main wing and flaps caused the disagreement between the computational and experimental results. These kinds of three-dimensional local flow separation affect the maximum lift and other aerodynamic forces. Careful validation and prediction of the flow separations are also required for the computations of realistic high-lift configurations.

References

[1] Rudolph PKC. "High-lift Systems on Commercial Subsonic Airliner," NASA CR 4746, Sept. 1996.

[2] Meredith, P. T., "Viscous Phenomena Affecting High-Lift Systems and Suggestions for Future CFD Development," *High-Lift Systems Aerodynamics*, AGARD CP 315, Sep. 1993, pp. 19-1 – 19-8.

[3] C. P. van DAM, "The aerodynamic design of multi-element high-lift systems for Transport Airplanes," *Progress in Aerospace Science*, Vol.38 101-144, 2002.

[4] C. B. McGinley, L. N. Jenkins, R. D. Watson and A. Bertelrud, "3-D High-Lift Flow-Physics Experiment –Transition Measurements," AIAA Paper 2005-5148, 2005.

[5] C. L. Rumsey and S. X. Ying, "Prediction of high lift: review of present CFD capability," *Progress in Aerospace Science*, Vol.38, 2002, pp. 145-180.

[6] Hansen, H., Thiede, P., Moens, F., Rudnik, R., and Quest, J., "Overview about the European High Lift Research Programme EUROLIFT," AIAA Paper 2004-0767, Jan. 2004.

[7] Lei, Z., Murayama, M., Takenaka, K., and Yamamoto, K., "CFD Validation for High-Lift Devices: Two-Element Airfoil," *Transactions of the Japan Society for Aeronautical and Space Sciences*, Vol. 49, No. 163, May 2006, pp. 31-39.

[8] Murayama, M., Lei, Z., Mukai, J., and Yamamoto, K., "CFD Validation for High-Lift Devices: Three-Element Airfoil," *Transactions of the Japan Society for Aeronautical and Space Sciences*, Vol. 49, No. 163, May 2006, pp. 40-48.

[9] Murayama, M., Yamamoto, K., and Kobayashi, K., "Validation of Computations Around High-Lift Configurations by Structured- and Unstructured-Mesh," *Journal of Aircraft*, Vol. 43, No.2 , March-April 2006, pp. 395-406.

[10] Murayama, M., Imamura, T., Yamamoto, K., and Kobayashi, K., "Comparison of RANS Simulations of Multi-Element High-Lift Configurations," AIAA Paper 2006-1396, Jan. 2006.

[11] http://db-www.larc.nasa.gov/trapwing/archive/register/ [cited 30 Dec. 2005]

[12] Johnson, P., Jones, K. M., and Madson, M., "Experimental Investigation of a Simplified 3D High Lift Configuration in Support of CFD Validation," AIAA Paper 2000-4217, Aug. 2000.

[13] Nash, S. M. And Rogers, S. E., "Numerical Study of a Trapezoidal Wing High-Lift Configuration," SAE Paper 1999-01-5559, Oct. 1999.

[14] Rogers, S. E., Roth, K., and Nash, S. M., "CFD Validation of High-Lift Flows with Significant Wind-Tunnel Effects," AIAA Paper 2000-4218, Aug. 2000.

[15] Chaffin, S. M. and Pirzadeh, S., "Unstructured Navier-Stokes High-Lift Computations on a Trapezoidal Wing," AIAA Paper 2005-5084, June. 2005.

[16] Ito, T., Ura, H., Yokokawa, Y., Kato, H., Mitsuo, K., and Yamamoto, K., "High-Lift Device Testing in JAXA 6.5m×5.5m Low-speed Wind Tunnel," AIAA Paper 2006-3643, June 2006.

[17] Yokokawa, Y., Murayama, M., Ito, T., and Yamamoto, K., "Experimental and CFD of a High-Lift Configuration Civil Transport Aircraft Model," AIAA Paper 2006-3452, June 2006.

[18] Ura, H., Yokokawa, Y., and Ito, T., "Phased Array Measurement of High Lift Devices in Low Speed Wind Tunnel," AIAA Paper 2006-2565, May 2006

[19] Imamura, T., Enomoto, S., and Yamamoto, K., "3D Unsteady Flow Computations in a Slat Cove Using Large Eddy Simulation," AIAA Paper 2006-2668, May 2006.

[20] Takaki, R., Yamamoto, K., Yamane, T., Enomoto, S. and Mukai, J., "The Development of the UPACS CFD Environment," *High Performance Computing, Proc. of ISHPC 2003*, Tokyo, Japan, Springer, pp. 307-319, 2003.

[21] Yamamoto, K., Ochi, A., Shima, E., and Takaki, R., "CFD Sensitivity of Drag Prediction on DLR-F6 Configuration by Structured Method and Unstructured Method," AIAA Paper 2004-0398, Jan. 2004.

[22] Shima, E., "A Simple Implicit Scheme for Structured/Unstructured CFD," *Proceedings of 29th Fluid Dynamics symposium,* Hokkaido, Japan, 1997, pp. 325-328. (in Japanese)

[23] Nakahashi, K., Togashi, F., Fujita, T., and Ito, Y., "Numerical Simulations on Separation of Scaled Supersonic Experimental Airplane from Rocket Booster at Supersonic Speed," AIAA Paper 2002-2843, June 2002.

[24] Murayama, M., Togashi, F., Nakahashi, K., Matsushima, K., and Kato, T. "Simulation of Aircraft Response to Control Surface Deflection Using Unstructured Dynamic Grids," *Journal of Aircraft*, Vol. 42, No. 2, March-April 2005, pp. 340-346.

[25] Ito, Y. and Nakahashi, K., "Surface Triangulation for Polygonal Models Based on CAD Data," *International Journal for Numerical Methods in Fluids*, Vol. 39, Issue 1, 2002, pp. 75-96.

[26] Sharov, D. and Nakahashi, K., "A Boundary Recovery Algorithm for Delaunay Tetrahedral Meshing," *Proceedings of 5th International Conference on Numerical Grid Generation in Computational Field Simulations*, Mississippi State, Mississippi, 1996, pp. 229-238.

[27] Ito, Y. and Nakahashi, K., "Improvements in the Reliability and Quality of Unstructured Hybrid Mesh Generation," *International Journal for Numerical Methods in Fluids*, Vol. 45, Issue 1, May 2004, pp. 79-108.

[28] Obayashi, S. and Guruswamy, G. P., "Convergence Acceleration of an Aeroelastic Navier-Stokes Solver," *AIAA Journal*, Vol. 33, No. 6, 1995, pp. 1134-1141.

[29] Sharov, D. and Nakahashi, K., "Reordering of Hybrid Unstructured Grids for Lower-Upper Symmetric Gauss-Seidel Computations," *AIAA Journal*, Vol. 36, No. 3, 1998, pp. 484-486.

[30] Spalart, P. R. and Allmaras, S. R., "A One-Equation Turbulence Model for Aerodynamic Flows," AIAA Paper 92-0439, Jan. 1992.

[31] Lei, Z., "Effect of RANS Turbulence Models on Computational of Separated Flows over a Wing-Body Configuration," *Transactions of the Japan Society for Aeronautical and Space Sciences*, Vol. 48, Nov. 2005, pp. 150-160.

[32] Matsuo, Y., Nakamura, T., Tsuchiya, M., Ishizuka, T., Fujita, N., Ohkawa, H., Hirabayashi, Y., Takaki, R., Yoshida, M., Nakamura, K., Yamamoto, K., Suematsu, K., and Iwamiya, T., "Numerical Simulator III – Building a Terascale Distributed Parallel Computing Environment for Aerospace Science and Engineering," *Proceedings of the Parallel CFD 2002 Conference*, Nara, Japan, Elsevier Science B. V., 2003, pp. 187-194.